DALHOUSIE
UNIVERSITY
Inspiring Minds

A One-Dimensional Cloud Model with Trimodal Convective Outflow

IAN FOLKINS

Department of Physics and Atmospheric Science, Dalhousie University, Halifax, Nova Scotia, Canada

ABSTRACT

The author describes a one-dimensional cloud model designed to investigate the relationships between stratiform downdrafts, congestus outflow, stability, and relative humidity in the tropical lower troposphere. In the tropics, the climatological lapse rate varies with height below the melting level in a way that is inconsistent with the assumptions of either moist pseudoadiabatic or reversible adiabatic ascent. This anomalous variation is referred to as the melting-level stability anomaly (MLSA). It is argued that the MLSA is caused by a transition from static to dynamic downdrafts at the melting level. Above the melting level, evaporation of precipitation cools and moistens the tropical atmosphere but does not generate downdraft parcels with sufficient negative buoyancy to descend between model levels. Below the melting level, the evaporative cooling associated with stratiform precipitation is strong enough to overcome the stability of the atmosphere and generate a convective-scale circulation. The vertical descent within these downdrafts induces a compensatory ascent in the background atmosphere that changes the overall cooling-to-moistening downdraft ratio. The inclusion of this stratiform downdraft circulation brings the modeled lapse rate and relative humidity profiles into simultaneous agreement with observations. The transition from static to dynamic downdrafts is triggered, in the model, by imposed increases in the amount of rain falling outside clouds, in the out-of-cloud rain rate, and in the vertical coherence of the rain shafts. The destabilization of the lower tropical atmosphere triggered by the stratiform circulation affects the development of convective clouds. In particular, the melting-level stability anomaly increases detrainment near the melting level and gives rise to the congestus mode.

1. Introduction

There are a number of interrelated aspects of convection in the tropical lower troposphere that are poorly simulated by most current models. Below the melting level (~5.5 km), the tropical lapse rate varies with height in a way that is inconsistent with moist adiabatic or pseudoadiabatic updraft parcel theory. Although these deviations from parcel theory may seem subtle, they have a strong effect on midtropospheric convective outflow. It has been recently recognized that there is a distinct convective outflow layer between 3 and 7 km associated with congestus type clouds (Johnson et al. 1999). Although there are some exceptions (Liu and Moncrieff 1998; Kuang and Bretherton 2006; Posselt et al. 2008), the congestus mode is poorly represented in many two- and three-dimensional models. The congestus mode is also not represented in most deep convective parameterizations, though it has been reproduced by the Emanuel parameterization (Emanuel and Zivkovic-Rothman 1999) when subject to a prescribed large-scale forcing (Bony and Emanuel 2001) and, to some extent, by the Gregory parameterization (Gregory and Rowntree 1990) when implemented in a climate model at high vertical resolution (Inness et al. 2001). Both the Emanuel and Gregory convective parameterizations are buoyancy-based parcel models. This paper describes a new buoyancy-based parcel model that successfully reproduces distinct boundary layer, congestus, and deep convective outflow modes as well as the stability anomaly at the melting level.

The paper is divided into sections. Section 2 is a brief overview of the model. Section 3 is a detailed discussion of the more technical aspects of the model. Section 4 is a discussion of the overall model performance, including heating rates, mass fluxes, and temperature and relative humidity profiles. The core of the original aspects of the paper is section 5, which discusses the origin of the melting-level stability anomaly and its relationship with congestus outflow. The final section is a summary.

Corresponding author address: Ian Folkins, Department of Physics and Atmospheric Science, Dalhousie University, Halifax, NS B3H 3J5, Canada.
E-mail: ian.folkins@dal.ca

2. Model overview

The model is run with interactive clear-sky radiation, a 24-h diurnal cycle, and a flux of heat and moisture from the surface. Updraft parcels are initiated from layers near the surface if the convective available potential energy (CAPE) of that layer is positive. It is desirable to generate a range of updraft parcel buoyancies and final detrainment heights. The starting updraft parcel spectrum of a layer is therefore given a range of initial moist static energy (h_m) and dry mass values. The mass-weighted mean h_m of the updraft spectrum is equal to the moist static energy of the background atmosphere at the initial altitude.

The updraft parcels are first forced to rise some initial distance. They then entrain air from the background atmosphere if their buoyancy increases with altitude. Conversely, they partially detrain into the background atmosphere if their buoyancy decreases with altitude. This buoyancy gradient mixing parameterization is not motivated by any theory of cloud-scale turbulence but by how an ensemble of clouds is expected to interact via gravity waves with a background atmosphere (Bretherton and Smolarkiewicz 1989). Updraft parcels fully detrain into the background atmosphere when their buoyancy becomes less than a particular threshold.

Updraft parcels generate rain when their condensate loading exceeds a prescribed upper limit. Some fraction of this updraft rain is assumed to fall through the unsaturated background atmosphere where it may evaporate and generate downdrafts. Downdraft parcels do not mix with the background atmosphere but may successively sink from one model level to the next, depending on the magnitude of their negative buoyancy. As a way of representing rainy stratiform anvils, the model prescribes a rapid increase in the fraction of rain falling through unsaturated air outside clouds near the melting level.

In the context of a one-dimensional model, it is difficult to physically represent the three-dimensional flows that give rise to rainy stratiform anvils, the weak updraft motions within stratiform anvils, the depositional growth and increased aggregation of ice crystals as they fall toward the melting level, their increase in size and fall speed, the rapid decrease in stratiform cloud area below the melting level, or the relative humidity of the ambient atmosphere below the melting level. At any height, the amount of evaporative cooling and moistening due to downdrafts can be expected to be affected by any of these processes, which can only be incorporated into one-dimensional cloud models in a parameterized manner. This introduces an unfortunate degree of freedom into the inclusion of downdrafts in cloud models of this type.

Although downdrafts can be affected by a number of processes that are difficult to quantify, the net effect of downdrafts on the background atmosphere, at a given height, can be characterized in terms of 1) a cooling rate and 2) a cooling-to-moistening ratio. We will argue that one can think of most downdrafts at a given height as being in one of two regimes. A downdraft parcel is considered to be in the static regime if the evaporative cooling within a downdraft parcel is not sufficient to overcome the stability of the atmosphere so that the downdraft parcel remains at its original model level. This could occur because either the atmosphere is locally too cold (i.e., saturated vapor pressure too small), the preexisting relative humidity of the parcel is too high, the rainwater mixing ratio is too small, the vertical coherence of the rainfall is small (so that the time over which the downdraft parcel is exposed to rain is small), or the local stability of the atmosphere is high. For static downdrafts, the cooling-to-moistening ratio is fixed by fundamental thermodynamic constants so that the net effect of a downdraft on the background atmosphere is entirely determined by the cooling rate. In the model, the cooling rate of static downdrafts at a given level is mainly determined by the local rate at which in-cloud rain is converted to out-of-cloud rain.

Downdraft parcels are considered to be in the dynamic regime if their negative buoyancy is sufficient to overcome the local atmospheric stability. In this case, downdraft parcels freely descend successively from one model level to the next. This type of downdraft gives rise to vertically overturning circulations in which the downdraft cooling-to-moistening ratio is no longer fixed by thermodynamic constants but is, instead, a property of the downdraft circulation as a whole and the background atmosphere.

In this model, all downdrafts above the melting level are static, and all downdrafts below the melting level are to some degree dynamic. The static to dynamic downdraft transition at the melting level is triggered by changes in prescribed rainfall properties and gives rise to significant changes in simulated lapse rates and cloud outflow. Within a particular downdraft regime, however, the effects of changes in prescribed rainfall properties on the model simulations are modest.

3. Model description

a. Specification of pressure levels

The thermodynamic variables of the model, including temperature T, water vapor mass mixing ratio r_v, and moist static energy h_m, are defined on fixed full pressure levels. The boundaries between full pressure levels are

referred to as half pressure levels. The surface pressure, or lowest half pressure level $p_{half}(1)$, is assigned an initial value 1000 hPa. For $p > 40$ hPa, the remaining half pressure levels are given by

$$p_{half}(i + 1) = p_{half}(i) - f_p^{i-1} \Delta p_{trop}. \quad (1)$$

In the standard version of the model, $\Delta p_{trop} = 50$ hPa and $f_p = 0.97$. The difference between half pressure levels is 50 hPa near the surface and 25 hPa near 100 hPa. The full pressure levels are given by

$$p(i) = 0.5(p_{half}(i + 1) + p_{half}(i)). \quad (2)$$

The model has 37 full levels, with 26 in the troposphere ($p > 100$ hPa). The model top is at 1.56 hPa. The temperature and relative humidity profiles generated by the model are essentially unchanged when the model is run at higher vertical resolution.

b. Surface heat and moisture fluxes

The heat and moisture fluxes at the surface are calculated according to bulk aerodynamic formulae. The temperature tendency of the lowest full level of the model due to a flux of heat from the surface is given by

$$\frac{dT(1)}{dt} = C_D |V| \frac{(T_{sst} - T(1))}{dz(1)}, \quad (3)$$

where $C_D = 0.002$ is a dimensionless exchange coefficient, $|V|$ is the surface wind speed, T_{sst} is the sea surface temperature, and $dz(1)$ is the thickness of the bottom layer. The water vapor mass mixing ratio tendency of the bottom model level is given by

$$\frac{dr_v(1)}{dt} = C_D |V| \frac{(r_{s,sst} - r_v(1))}{dz(1)}, \quad (4)$$

where $r_{s,sst}$ is the saturated water vapor mixing ratio at the ocean temperature and surface pressure.

c. Radiative cooling

The clear-sky radiative cooling rate is calculated interactively every time step using a radiative transfer model (Fu and Liou 1992), and the most recent temperature and water vapor mixing profiles of the model as inputs. In the default version of the model, the ozone profile is fixed at a tropical annual mean profile generated using 12 stations from the Southern Hemisphere Additional Ozonesondes (SHADOZ) archive (Thompson et al. 2003).

d. Mass flux closure

Updraft parcels originate from model levels near the surface with positive reversible density CAPE. CAPE is calculated in the standard way, except that the contributions from model levels closer to the surface are weighted more strongly. This makes the updraft mass flux less responsive to changes in the background temperature of the upper troposphere:

$$cape_d(n) = \sum_{i=n}^{LNB} e^{-z(i)/z_{scale}} (T_{dp}(i, n) - T_v(i)) R_d d \ln p(i). \quad (5)$$

The sum over i extends from near surface layer n to the level of neutral buoyancy (LNB), $T_v(i)$ is the virtual temperature of the background atmosphere at layer i, and $T_{dp}(i, n)$ is the density temperature of a parcel starting from layer n, lifted reversibly to layer i. The density temperature takes into account the effects of condensate loading and water vapor on density. The weighting parameter z_{scale} is set equal to 5000 m; $p(i)$ is the pressure of full level i; and R_d is the gas constant for dry air.

Convection is initiated from a layer n near the surface when $cape_d(n) > 0$. The total number of updraft parcels released from a level per time step is n_{launch}. In these simulations $n_{launch} = 16$. The total dry mass of all n_{launch} parcels is given by

$$m_{d,up,all}(n) = \left(\frac{t_{step}}{t_{scale}}\right) \left(\frac{cape_d(i)}{cape_{scale}}\right) \left(\frac{dp_d(n)}{g}\right), \quad (6)$$

where (with default values in brackets) t_{step} is the time step of the model (20 min), t_{scale} is a prescribed time scale over which convection is assumed to remove positive CAPE air from the boundary layer (6 h), $cape_{scale}$ is a parameter that sets the scale of CAPE in the boundary layer (200 J kg^{-1}), g is the gravitational acceleration, and $dp_d(i)$ is the dry pressure increment of layer n:

$$dp_d(n) = \frac{dp(n)}{(1 + r_v(n))}. \quad (7)$$

In these models runs, $cape_d(1) \sim 80$ J kg^{-1}, so that convection typically removes about 2.2% of the mass in the bottom layer every 20-min time step. The updraft mass flux and mean rainfall will typically increase in response to increases wind speed and sea surface temperature.

e. Updraft parcel mass and moist static energy spectrum

The moist static energy per unit dry mass of a parcel can be defined (Emanuel 1994)

$$h_{mp}(T_p, r_{vp}, r_{ip}, r_{tp}, z) \equiv (c_{pd} + r_{tp}c_l)T_p + l_v(T_p)r_{vp}$$
$$- l_f(T_p)r_{ip} + (1 + r_{tp})gz, \quad (8)$$

where c_{pd} is the specific heat of dry air, c_l the specific heat of liquid water, T_p the air parcel temperature, $l_v(T_p)$ the latent heat of vaporization, $l_f(T_p)$ the heat of melting, z the altitude, r_{vp} the water vapor mass mixing ratio, r_{ip} the ice mass mixing ratio, and r_{tp} the total water mass mixing ratio. The liquid water mass mixing ratio of the parcel can be defined $r_{lp} = r_{tp} - r_{vp} - r_{ip}$. The model is formulated in such a way that cloud ice and snow are permitted. However, the simulations discussed here do not consider this possibility (i.e., $r_{ip} = 0$ always).

Equation (6) specifies the total mass of all updraft parcels from a convecting level during a time step. This total mass is divided into a number n_{launch} parcels of varying mass and moist static energy. The introduction of an updraft mass and moist static energy spectrum is an attempt to represent subgrid-scale variability and to generate a range of updraft outflow altitudes. The moist static energy h_m of the updraft parcels at starting level n were assumed to be equally distributed between $h_m(n) - 0.5\Delta h_m$ and $h_m(n) + 0.5\Delta h_m$, where $\Delta h_m = 4$ kJ kg^{-1}. Let n_l refer to a parcel index ranging from 1 to n_{launch}, and the parameter f_u have the definition

$$f_u = \frac{(n_l - 1)}{(n_{\text{launch}} - 1)}. \qquad (9)$$

Here f_u ranges from 0 to 1 and specifies the position of a parcel within the updraft h_m spectrum. The equally spaced moist static energy spectrum of the updraft parcels starting at level n is then given by

$$h_{mp}(n, n_l) = h_m(n) + (f_u - 0.5)\Delta h_m. \qquad (10)$$

Each updraft parcel is assumed to have the same initial relative humidity. To conserve total water, the dry mass-weighted mean r_{vp} of the parcel spectrum is constrained to equal the background r_v of the initial layer.

The probability distribution function of moist static energy in the boundary layer is roughly triangular (Folkins and Braun 2003). We therefore adopt a triangular mass spectrum in which the mass of the two parcels with the lowest and highest moist static energy (i.e., $n_l = 1$ and $n_l = n_{\text{launch}}$) is m_{ratio} times smaller than the mass of the parcel whose h_m is at the center of the moist static energy spectrum (i.e., has $f_u = 0.5$). The total initial dry mass of all updraft parcels is constrained to equal $m_{d,\text{up,all}}(n)$, as defined in Eq. (6).

Every updraft parcel with positive reversible CAPE is forced to rise some initial distance z_{up} (800 m) from its starting level. After this forced ascent, parcels may spontaneously rise and mix with the background atmosphere. Parcels fully detrain into the background atmosphere once their buoyancy becomes less than b_{detrain}. In these simulations, $b_{\text{detrain}} = -0.01$ m s^{-2} so that updraft
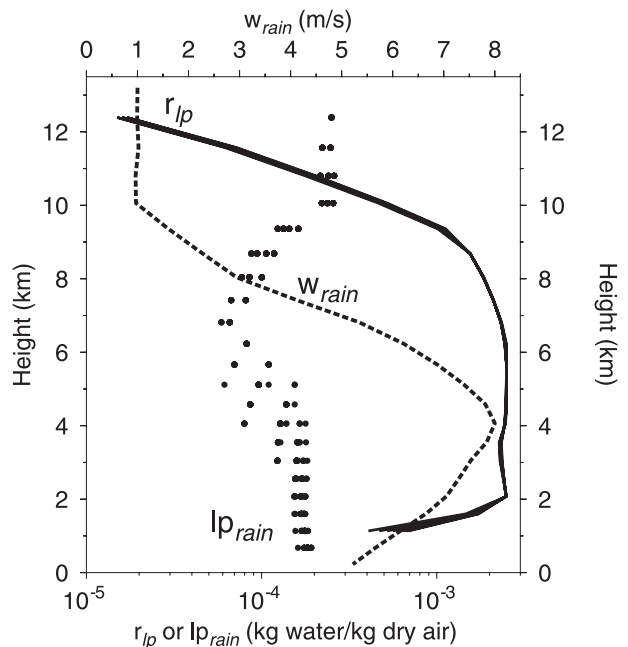

FIG. 1. The dashed curve shows the prescribed dependence of the rain velocity w_{rain} on height in the model. Solid black circles refer to the rainwater mixing ratio lp_{rain} of various rain shafts. The solid black curve shows the updraft condensate loading r_{lp} of the updraft parcels.

parcels are permitted to be weakly negatively buoyant (Jorgensen and LeMone 1989).

f. Rain formation

At each model level, any liquid water condensate in excess of a prescribed threshold is removed from the updraft parcel and considered to be rain. This threshold is given by

$$r_{l,\text{max}} = \min(r_{l,\text{const}}, r_{l,\text{ratio}} r_{sp}(i)), \qquad (11)$$

where $r_{l,\text{const}}$ and $r_{l,\text{ratio}}$ are temperature dependent constants and $r_{sp}(i)$ is the saturated water vapor mixing ratio of a parcel at level i. In practice, at lower altitudes, the maximum liquid water content is effectively fixed at $r_{l,\text{const}}$. At upper altitudes, it is fixed at some fraction of the saturated water vapor mass mixing ratio of the updraft parcel. Figure 1 shows vertical profiles of the updraft condensate r_{lp} in the model generated by implementing a prescribed variation in $r_{l,\text{max}}$; $r_{l,\text{max}}$ is approximately constant at 0.0025 (kg of cloud water kg^{-1} of dry air) below 8 km and rapidly decreases above this altitude. At some altitudes, condensate detrainment makes a significant contribution to the water vapor budget. The variation in $r_{l,\text{max}}$ is therefore tuned, in part, to generate a mean relative humidity profile in agreement with observations.

In particular, in the absence of reasonably large values of $r_{l,\max}$ to ~10 km, the simulated relative humidity of the model in the 6–10-km height interval would be too dry.

g. Updraft mixing

Updraft parcels are lifted vertically in such a way as to conserve moist static energy h_{mp} and total water r_{tp}. Parcels are not permitted to mix for some initial distance from their starting level ($z_{\text{nomix}} = 800$ m). Otherwise, once an air parcel has ascended to the next highest level and has had possible condensate removal associated with rain formation, it undergoes buoyancy gradient mixing (Bretherton and Smolarkiewicz 1989). Buoyancy gradient mixing is designed to damp changes in the vertical buoyancy gradient of an updraft and helps equilibrate convective updrafts and the background atmosphere toward a common density profile.

The updraft parcel buoyancy at level i is calculated using

$$b_p(i) = g\frac{(T_{\text{dp}}(i) - T_v(i))}{T_v(i)}. \qquad (12)$$

At any model level i, one could define a buoyancy gradient with respect to the adjacent level at $i \pm 1$. The model calculates the buoyancy gradient with respect to both levels and does backward and forward buoyancy gradient mixing. The backward mixing coefficient is given by

$$\sigma_{\text{back}} = \frac{n_{\text{launch}}}{n_l}\frac{b_p(i) - b_p(i-1)}{b_{\text{scale}}}, \qquad (13)$$

where $b_p(i)$ is the parcel buoyancy at level i prior to condensate removal; $b_p(i-1)$ is the parcel buoyancy at the previous lower level, after mixing and condensate removal at that level; b_{scale} is a parameter that helps set the updraft buoyancy scale. Smaller values of b_{scale} increase updraft entrainment and detrainment and tend to increase the relative humidity of the background atmosphere. Here $b_{\text{scale}} = 0.23$ m s^{-2}.

The introduction of the n_{launch}/n_l ratio in Eq. (13) is intended to decrease the mixing of the most energetic updraft parcels (those with larger n_l). In the absence of this ratio, the parcels with largest initial h_{mp} will have the largest buoyancy, the largest buoyancy gradients, and the largest σ_{back} mixing coefficients. Buoyancy gradient mixing would then quickly narrow the spread in any initial h_{mp} updraft parcel spectrum so that all updraft parcels would evolve in a similar manner and detrain at a similar height. In the model, the introduction of this ratio is needed to give a spread in updraft outflow altitudes.

An updraft parcel entrains a mass Δm_d of dry air from the background atmosphere when $\sigma_{\text{back}} > 0$ (increasing buoyancy) and detrains a mass Δm_d of dry air into the background atmosphere when $\sigma_{\text{back}} < 0$ (decreasing buoyancy). The change in mass Δm_d is calculated from σ_{back} using

$$\sigma_{\text{back}} = \frac{\Delta m_d}{\Delta m_d + m_{d,\text{up}}} \qquad (14)$$

in which $m_{d,\text{up}}$ refers to the dry mass of the updraft parcel before mixing. In the case of entrainment, the new mixed moist static energy and total water mass mixing ratio of the parcel are given by

$$h'_{mp} = \sigma_{\text{back}}h_m(i) + (1 - \sigma_{\text{back}})h_{mp}(i), \qquad (15)$$

$$r'_{tp} = \sigma_{\text{back}}r_v(i) + (1 - \sigma_{\text{back}})r_{tp}(i). \qquad (16)$$

The new $T_p(i)$, $r_{vp}(i)$, and $r_{lp}(i)$ of the mixed updraft parcel can then be determined from h'_{mp} and r'_{tp}. In the case of detrainment, the dry mass of the updraft parcel is reduced but the parcel properties are otherwise unchanged.

The forward updraft buoyancy gradient mixing coefficient is given by

$$\sigma_{\text{for}} = \frac{n_{\text{launch}}}{n_l}\frac{b_p(i+1) - b_p(i)}{b_{\text{scale}}}. \qquad (17)$$

Here $b_p(i)$ is the buoyancy of the updraft air parcel at level i after both condensate removal and backward buoyancy gradient mixing, and $b_p(i+1)$ is the buoyancy the parcel at level i would have after undergoing a "virtual" ascent to level $i+1$.

The value of $b_p(i+1)$ in Eq. (17) is sensitive to the treatment of condensate in going from level i to level $i+1$. In reversible ascent, all condensate is assumed to be retained. This assumption tends to reduce $b_p(i+1)$ and favor detrainment. Alternatively, one could assume that condensate is removed according to Eq. (11). This assumption would increase the buoyancy at $i+1$ and favor entrainment. In practice, some compromise between the two assumptions appears to work best. For the purpose of calculating $b_p(i+1)$ in Eq. (17), the condensate loading at $i+1$ is assumed to equal

$$r_l(i+1) = f_{\text{for}}r_{l,\max}(i+1) + (1 - f_{\text{for}})r_{l,\text{rev}}(i+1). \qquad (18)$$

Here $r_{l,\max}(i+1)$ is the condensate loading at $i+1$ calculated using Eq. (11), and $r_{l,\text{rev}}(i+1)$ is the reversible condensate loading at $i+1$. The parameter f_{for} is used to interpolate between these assumptions and is set equal to 0.6.

There are clearly a number of ambiguities in the implementation of buoyancy gradient mixing. In the backward mixing calculation, one could calculate $b_p(i)$ before or after condensate removal at that level. In the forward mixing calculation, one could calculate $b_p(i)$ before or after backward mixing and make various assumptions on the condensate loading at level $i + 1$. These choices can have a significant impact on the model simulations and are resolved here mainly by a process of determining which choices generate the most realistic temperature and relative humidity profiles.

h. Geometry and mass loading of rain shafts

The model converts any cloud condensate in excess of a prescribed maximum, as given by Eq. (11), to rain. Because the production of rain occurs within model layers, rain is considered a half-level variable, that is, defined at the boundaries between model layers. It is initially assumed that all rain remains within the cloud. At each height, however, some fraction of the in-cloud rain is converted to out-of-cloud rain. The fractional rate of conversion per kilometer of in-cloud rain to out-of-cloud rain is referred to as f_{rem} and is specified as a function of temperature. The dashed curve in Fig. 2 shows the dependence of f_{rem} on altitude in the model. The rapid increase in f_{rem} near 0°C is intended to represent the exit of stratiform rain from the base of rainy stratiform anvils.

The rainwater mass (kg water m^{-2}) that exits a cloud at a model level is equally divided into num$_{shaft}$ rain shafts of different lengths. The mean rain shaft length is specified as a function of temperature and plotted against altitude in Fig. 2. It is assumed that there is a rapid increase in the vertical coherence of rain shafts near the melting level. At each level, the longest rain shaft is assumed to be dz_{shaft} times longer than the shortest. The lengths of the remaining rain shafts are geometrically distributed between the shortest and longest. In these model runs, num$_{shaft}$ = 10 and dz_{shaft} = 6. The main reason for using a variety of rain shaft lengths at every exit level is to introduce additional variance into the downdraft parcel trajectories.

Rain shafts that exit a cloud are assumed to have a particular local rain rate (kg water m^{-2} s^{-1}). The value of rn_{rate} is determined by the temperature of the model level at which the rain shaft exits the cloud. The dependence of rn_{rate} on the altitude of origin is shown in Fig. 2. The rain rate of a rain shaft is assumed to be constant as it falls toward the surface.

The terminal fall speed w_{rain} of a raindrop depends mainly on the raindrop size and the local atmospheric density (e.g., Fowler et al. 1996). The dependence of w_{rain} on height used in the model is shown in Fig. 1. This
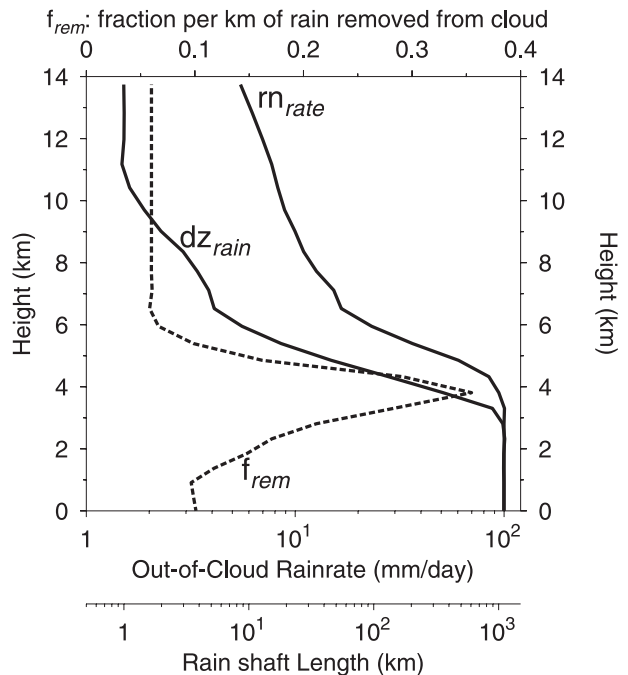

FIG. 2. The thick dashed line shows the fractional rate of conversion f_{rem} of in-cloud rain to out-of-cloud rain. The solid black lines refer to the prescribed out-of-cloud rain rate rn_{rate} and rain shaft length dz_{rain}.

fall speed is intended to be a representative average for out-of-cloud rain. For constant raindrop size, one would expect w_{rain} to increase with altitude. Above the melting level, however, w_{rain} should decrease in response to a reduction in mean hydrometeor size. Realistic changes in the prescribed raindrop fall speed do not appear to have a significant effect on the model simulations.

The rainwater mass mixing ratio $lp_{rain}(i)$ (kg rain kg^{-1} dry air) of a rain shaft at model level i that exited a cloud at model level i_{exit} is given by

$$lp_{rain}(i) = \frac{rn_{rate}(i_{exit})}{w_{rain}(i)\rho_d(i)} \qquad (19)$$

in which $\rho_d(i)$ refers to the background dry air density at level i. Figure 1 shows the variation in rainwater mass mixing ratios of various rain shafts as a function of altitude. At a given height, the variation in $lp_{rain}(i)$ is due to changes in the imposed rain rate at the different exit altitudes.

The starting water mass of a rain shaft can be expressed in terms of the total in-cloud rain at the exit level, the fractional removal rate per kilometer of the in-cloud rain at that exit level, the width of the exit grid cell, and the total number of rain shafts originating at that level:

$$\text{mass}_{\text{shaft}}(i_{\text{exit}}) = \frac{\text{rain}_{\text{in}}(i_{\text{exit}})f_{\text{rem}}(i_{\text{exit}})\,dz(i_{\text{exit}})}{\text{num}_{\text{shaft}}}. \qquad (20)$$

This rain mass can be used to assign a dimensionless fractional area to every rain shaft:

$$\text{area}_{\text{shaft}}(i_{\text{exit}}) = \frac{\text{mass}_{\text{shaft}}(i_{\text{exit}})}{lp_{\text{rain}}(i_{\text{exit}})\,dz_{\text{shaft}}(i_{\text{exit}})}. \qquad (21)$$

The areal fraction of the grid cell occupied by a rain shaft is proportional to the mass of the rain shaft and inversely proportional to the rainwater mass mixing ratio and imposed length.

Rain shafts evaporate as they fall toward the ground. The mass of a rain shaft at some model level i for $i < i_{\text{exit}}$ will therefore be less than $\text{mass}_{\text{shaft}}(i_{\text{exit}})$. For $i < i_{\text{exit}}$ the rainwater mass mixing ratio $lp_{\text{rain}}(i)$ in Eq. (21) is constrained by Eq. (19). Reductions in the mass of a rain shaft as it falls toward the surface must therefore be compensated by some reduction in the fractional area or length of the shaft. Here we assume that the fractional area of a rain shaft is fixed at its exit value. Evaporation of a rain shaft therefore gives rise to reductions in rain shaft length.

i. Downdraft parcel initiation and descent

At every exit level, the fractional area of each rain shaft defines a subcolumn of the background atmosphere. At levels at and below the exit level, this fractional area is used to define the dry mass entrained from the background atmosphere into a downdraft parcel:

$$m_{d,dn}(i) = \frac{\text{area}_{\text{shaft}}(i_{\text{exit}})\,dp_d(i)}{g}. \qquad (22)$$

The dry pressure increment $dp_d(i)$ of layer i is defined in Eq. (7). A rain shaft is then subdivided into $\text{num}_{\text{layers}} = 15$ layers. Each of these rain shaft layers successively falls through the downdraft parcels in the subcolumn beneath it. The rate of change of water vapor mixing ratio $r_{vp}(i)$ within each downdraft parcel due to evaporation from the rain shaft layer is determined using a parameterized expression (Emanuel 1991):

$$E_v(i) = \frac{(1 - r_{vp}(i)/r_{sp}(i))\sqrt{lp_{\text{rain}}(i)}}{2000 + 10^4/(0.01p(i)r_{sp}(i))}, \qquad (23)$$

where $p(i)$ refers to the local pressure (Pa), and $r_{sp}(i)$ is the saturated water vapor mass mixing ratio of the downdraft parcel. The mass mixing ratio $lp_{\text{rain}}(i)$ of a rain shaft layer is recalculated at every height as the layer falls to the surface using Eq. (19). The increase in water vapor mass mixing ratio for the downdraft parcels is given by

$$dr_{vp}(i) = E_v(i)t_{evap}(i). \qquad (24)$$

The time t_{evap} over which the downdraft parcel is exposed to the rain shaft layer is given by

$$t_{evap}(i) = \frac{dz_{\text{layer}}(i)}{w_{\text{rain}}(i)}. \qquad (25)$$

The layer thickness $dz_{\text{layer}}(i)$ is calculated using an expression similar to Eq. (21) except that the rainwater mass of a layer, rather than an entire shaft, is used. The water mass of a layer is updated after every evaporation event, with $dz_{\text{layer}}(i)$ reduced accordingly. A rain shaft layer may entirely evaporate as it falls toward the surface. Alternatively, some fraction of the initial mass of a rain shaft layer may reach the surface. The relative humidity of the downdraft parcels tends to increase as rain shaft layers sequentially pass through them. This gives rise to a reduction in the evaporation of subsequent layers so that the uppermost layers of a rain shaft tend to fall farther than those near the bottom of a rain shaft. For numerical reasons, the relative humidity of a downdraft is not allowed to reach 100% but is assigned a maximum value of 0.96.

After the evaporation associated with the passage of a rain shaft layer, the density temperature T_{dp} of a downdraft parcel is recalculated:

$$T_{dp}(i) = \frac{T_p(i)(1 + (r_{vp}/\epsilon))}{1 + r_{vp}(i) + lp_{\text{rain}}(i)}. \qquad (26)$$

The downdraft parcel buoyancy $b_p(i)$ is then determined using Eq. (12). Downdraft parcels are moved downward one level if their negative buoyancy is large enough to overcome the stability of the atmosphere. This is determined by first virtually advecting the parcel down one level and calculating buoyancy $b_p(i - 1)$ at level $i - 1$. The average of the buoyancies at i and $i - 1$ is called the dynamical buoyancy:

$$b_{\text{dyn}} = 0.5(b_p(i) + b_p(i - 1)). \qquad (27)$$

Downdraft parcels are moved from level i to $i - 1$ if $b_{\text{dyn}} < 0$. The maximum number of evaporation events a downdraft may experience in a time step is $\text{num}_{\text{layers}}$. The maximum number of downward movements a downdraft parcel may experience within a time step is also equal to $\text{num}_{\text{layers}}$. If a downdraft parcel reaches the surface, it does not descend any further. It may, however, continue to be evaporatively cooled, if additional rain shaft layers pass through it, prior to detrainment into the bottom model level. Owing to differing vertical

motions of downdraft parcels under a rain shaft, a rain shaft layer may evaporate into multiple downdraft parcels at a given model level, or none.

j. Brewer–Dobson circulation

Above 15 km, the Brewer–Dobson circulation plays an increasingly important role in regulating tropical temperature and chemical species profiles (Fueglistaler et al. 2009). The model imposes this circulation via a specified input of dry air between 400 and 200 hPa with the same mass of dry air removed from the model column between 40 and 5 hPa. Air being added or removed from the model is assumed to have the same water vapor mixing ratio as the ambient background profile. Because air is dehydrated as it rises up through the tropical tropopause, the imposition of the Brewer–Dobson circulation is associated with an external source of moisture to the model. This external moisture source is quite small, however, as the default Brewer–Dobson mass flux is specified as 27.3 Pa day^{-1} (Rosenlof and Holton 1993), or approximately 100 times smaller than the overturning convective circulation. The Brewer–Dobson circulation is turned on in all simulations, except for those discussed in section 3m.

k. Calculation of the convective temperature and moisture tendencies

Updraft and downdraft parcels transport h_m and r_t vertically and mediate the exchange of h_m and r_t between the rain shafts and the background atmosphere. Briefly, the rates of change in the background temperature and water vapor mixing ratio profiles due to this vertical transport and mixing are calculated as follows.

It is assumed that there is no vertical flux of mass, h_m, or r_t through the top of the model. Entrainment and detrainment from updrafts and downdrafts occurring at a model level will add or remove moist static energy h_m, total water r_t, and dry mass m_d. The model calculates the residual (total) sum of each quantity. The net change in total mass (dry air plus water vapor) of the layer due to updraft and downdraft addition and removal can then be calculated. The pressure increment $dp(i)$ and total mass of each layer are kept fixed. This constraint can be used to calculate the required flux of mass through the lower boundary of the layer. In the case of a need for an induced downward transport of air through the lower boundary of layer i, the r_v and h_m of the subsiding air are assumed equal to the initial background values at layer i. Similarly, when there is an induced upward flux of air across the lower boundary of layer i from layer $i - 1$, the h_m and r_v of the ascending air assume the values of their layer of origin. The model then calculates a new mixed total h_m, r_t, and m_d in layer i resulting from all horizontal

updraft and downdraft inflows and outflows and vertical fluxes at the top and bottom boundaries. The new temperature and water vapor mixing ratio of the layer can then be calculated. The model successively works its way to the surface, using the solution at the lower boundary of layer i as an upper boundary condition for the solution of layer $i - 1$.

Note that, with the above procedure, all pressure levels of the model are fixed except the surface pressure $p_{\text{half}}(1)$. While the total dry mass of the model is fixed, there will be a net reduction in column water when convection generates rainfall that reaches the surface. Within a time step, the associated reduction in surface pressure will be at least partially offset by a surface flux of water vapor and a small net amount of water vapor added to the model associated with the imposed Brewer–Dobson circulation. The surface pressure will converge to a constant value as radiative convective equilibrium is approached and the 24-h averaged column water becomes time independent. Within a 24-h period, the diurnal cycle in rainfall gives rise to a diurnal cycle in column water, surface evaporation, and surface pressure.

l. Moist static energy of rain

The total column moist static energy of all in-cloud and out-of-cloud rain is called $H_{m,\text{rain}}$ (J m^{-2}); $H_{m,\text{rain}}$ is increased when the condensate r_l of an updraft parcel exceeds the local precipitation threshold $r_{l,\text{max}}$, and it is decreased during evaporation within downdrafts:

$$
H_{m,\text{rain}} = \sum_{r_l > r_{l,\text{max}}}^{\text{precip}} m_{d,\text{up}}(c_l T_{p,\text{up}} + g z_{p,\text{up}})(r_{l,\text{up}} - r_{l,\text{max}})
$$
$$
- \sum_{\Delta r_{d,\text{dn}} > 0}^{\text{evap}} m_{d,\text{dn}}(c_l T_{p,\text{dn}} + g z_{p,\text{dn}}) \Delta r_{d,\text{dn}}. \quad (28)
$$

In this expression, $T_{p,\text{up}}$, $z_{p,\text{up}}$, $r_{l,\text{up}}$, and $m_{d,\text{up}}$ refer to the updraft parcel temperature, height, liquid water mass mixing ratio, and dry mass (similarly for the downdraft parcels); $\Delta r_{d,\text{dn}}$ refers to an increase in downdraft water vapor mixing ratio due to rainfall evaporation. The model does not attempt to explicitly convert the gravitational potential energy of rain to rain kinetic energy as it falls or dissipate the kinetic energy of the rain as heat. It also makes the assumption that, when evaporation occurs, the moist static energy of the rain is reduced as if the rain were at the same temperature and height as the downdraft air parcel. The model therefore makes no attempt to account for possible increases in downdraft cooling rates associated with increasing the temperature of the rain in a rain shaft to the temperature of the

downdraft parcel through which it is falling. These simplifications in the moist static energy budget of the rain are not likely to have a significant effect on the simulations.

m. Enthalpy and water conservation

The moist static energy of a parcel is a sum of the moist enthalpy k_m and gravitational potential energy (Emanuel 1994):

$$h_m = k_m + (1 + r_t)gz. \qquad (29)$$

Moist enthalpy is added to the model atmosphere via surface heat and moisture fluxes. It is removed from the model mainly via radiative cooling and precipitation. In the absence of mass transport across the boundaries, moist convection converts latent enthalpy into gravitational and internal energy but leaves the vertically integrated column moist enthalpy unchanged. The column moist enthalpy per unit area can be calculated by multiplying the moist enthalpy of every layer by the dry mass per unit area and summing over all model layers:

$$K_m = \left(\frac{1}{g}\right)\sum_{i=1}^{n} k_m(i) \, dp_d(i). \qquad (30)$$

If the Brewer–Dobson circulation is turned off, the initial column enthalpy $K_{m,i}$ prior to the convective portion of a time step should equal the sum of the column enthalpy $K_{m,f}$ after convection plus the enthalpy lost from the model via transport of rain through the bottom level. The loss of enthalpy via rain exiting the column is equal to the rain moist static energy as calculated as in Eq. (28), with the understanding that the gravitational potential energy of the rain is converted to rain internal energy as it descends (i.e., increasing the effective temperature of the rain):

$$K_{m,i} = K_{m,f} + H_{m,\text{rain}}. \qquad (31)$$

Within each model time step, there are several hundred events in which parcels are advected vertically, mixed, or exposed to evaporative cooling. The numerical routines used by the model enforce conservation of moist static energy and total water during each event and iteratively solve for the final temperature and water vapor mixing ratio. They are effectively forced to allow for some small inconsistency between the r_v and r_s of saturated air parcels, the size of the inconsistency depending on the number of iterations. This inconsistency is preferable to the introduction of errors into conserved quantities.

Figure 3 shows the diurnal variation of some of the terms in the column and moist enthalpy budgets of the model during a simulation in which the Brewer–Dobson
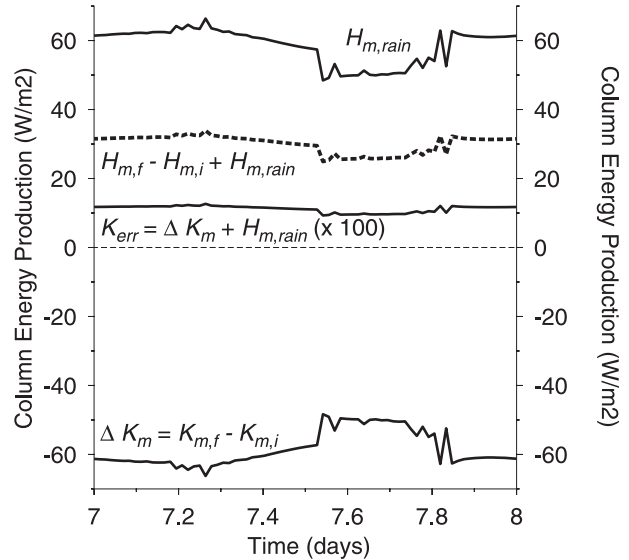

FIG. 3. Terms in the energy budget of the model during day 7 of a simulation in which the Brewer–Dobson circulation is turned off. The solid curve at bottom denoted ΔK_m refers to the decrease in column enthalpy due to convection. To the extent that the model exactly conserves column enthalpy, this decrease should be balanced by the rain enthalpy exiting the bottom of the model. This loss is denoted $H_{m,\text{rain}}$. The column enthalpy error due to convection in the model is denoted K_{err}, for clarity multiplied by 100. The dashed line refers to the increase in column moist static energy during convection due to an increase in gravitational potential energy.

circulation is turned off. The residual column enthalpy error K_{err} of the model is ~ 0.1 W m^{-2}. This is roughly equivalent to an error in column temperature of 0.001 K day^{-1} (about 1000 times smaller than the convective tendencies). The loss of moist static energy from the model due to rain exiting the column during convection is ~ 50 W m^{-2}. The net production of ~ 25 W m^{-2} of moist static energy during convection is due to an increase in column gravitational potential energy and is a reflection of the hydrostatic redefinition of $z(i)$ during convection.

n. Buoyancy work

The model does not explicitly account for the dissipation of parcel kinetic energy. This source of enthalpy is, however, implicitly accounted for by the imposition of moist static energy conservation during parcel vertical displacements.

During an adiabatic process, there is a change dK in enthalpy associated with a pressure change dp:

$$dK_m = V \, dp. \qquad (32)$$

Dividing both sides by the dry mass m_d gives

$$dk_m = \frac{dp}{\rho_d}, \tag{33}$$

where k_m is the specific enthalpy per unit dry mass, and $\rho_d = m_d/V$ is the dry air density. The total density can be expressed in terms of the dry air density or, alternatively, as a sum of a hydrostatic (i.e., background) density and a small deviation:

$$\rho_t = (1 + r_t)\rho_d = \rho_{\mathrm{hyd}} + \delta\rho \tag{34}$$

Using Eq. (34) for ρ_d in Eq. (33) gives

$$dk_m = \frac{(1 + r_t)\,dp}{\rho_{\mathrm{hyd}}(1 + \delta\rho/\rho_{\mathrm{hyd}})}. \tag{35}$$

When $\delta\rho/\rho_{\mathrm{hyd}} \ll 1$, and using the hydrostatic relation $dp = -\rho_{\mathrm{hyd}}g\,dz$,

$$dk_m = -(1 + r_t)g\,dz + \frac{(1 + r_t)g\delta\rho\,dz}{\rho_{\mathrm{hyd}}}. \tag{36}$$

Using Eq. (29), this can be written

$$dh_m = -(1 + r_t)gB_p\,dz, \tag{37}$$

where $B_p = -\delta\rho/\rho_{\mathrm{hyd}}$ is the parcel buoyancy. Rather than using Eq. (37), the model imposes $dh_m = 0$ during the nonhydrostatic vertical displacement of updraft and downdraft air parcels. This is equivalent to adding a source of moist static energy to vertically displaced air parcels equal to the buoyancy work done on the air parcel, or effectively making the assumption that all parcel kinetic energy is immediately dissipated. For the purposes of the column enthalpy budget, it is therefore not necessary to explicitly calculate the kinetic energy of updraft and downdraft air parcels.

4. Model performance

a. Updraft and downdraft mass fluxes

The model is typically run for 42 days to reach radiative convective equilibrium. Results are diurnally averaged over the last 10 days of a simulation. Figure 4 shows the updraft ω_{up} and downdraft ω_{dn} mass fluxes associated with the vertical movement of updraft and downdraft parcels between model levels. Figure 4 also shows the induced mass flux ω_{ind}. This is the mass transport between model levels required to keep the total mass between any two pressure half levels constant. In the real atmosphere, the induced descent (in the case of updrafts), or induced ascent (in the case of downdrafts), would occur within some horizontal distance of a convective event.
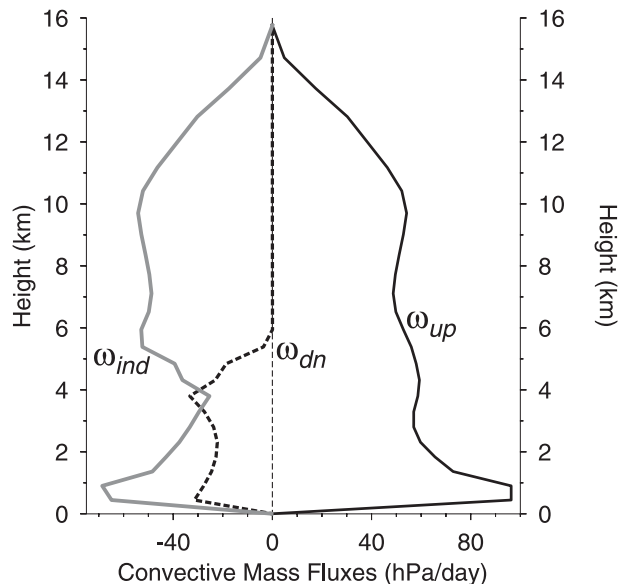

FIG. 4. The mass fluxes of the model due to updrafts ω_{up} (solid black) and downdrafts ω_{dn} (dashed black). The induced mass flux ω_{ind} (solid gray) is the vertical mass flux required to keep the amount of mass between the model pressure levels fixed.

Figure 4 shows that there is a rapid increase in the downdraft mass flux below 6 km. This increase would contribute to the convergent inflow toward mesoscale convective systems near the melting level, as observed by aircraft radar (Mapes and Houze 1995). In the model, this increase is mainly due to imposed changes in the out-of-cloud rain rate and the imposed rain shaft geometry. In the upper troposphere, the out-of-cloud rain shafts have small vertical thickness and small rain rates. Rain shafts are distributed over a large horizontal fractional area, as are the downdraft parcels they entrain from the background atmosphere. The increase in downdraft water vapor mass mixing ratio r_v due to the passage of a rain shaft layer through a downdraft parcel is proportional to the exposure time t_{evap}. The exposure times of updraft parcels exposed to vertically thin rain shaft layers (small dz_{layer}) are small. This reduces the net moistening and cooling of downdraft parcels exposed to rain shaft layers originating in the upper troposphere. As a result, the buoyancies of upper-tropospheric downdrafts are weak and rarely sufficient to overcome the stability of the atmosphere. Instead, downdraft parcels detrain into the background atmosphere at the same level as they were entrained. Evaporation of rain locally cools and moistens the atmosphere but does not give rise to a downdraft mass flux or any induced upward motion in the background atmosphere. This type of downdraft is referred to as "static."

The model imposes rapid increases in the out-of-cloud rain rate and rain shaft length below 6 km. The evaporative
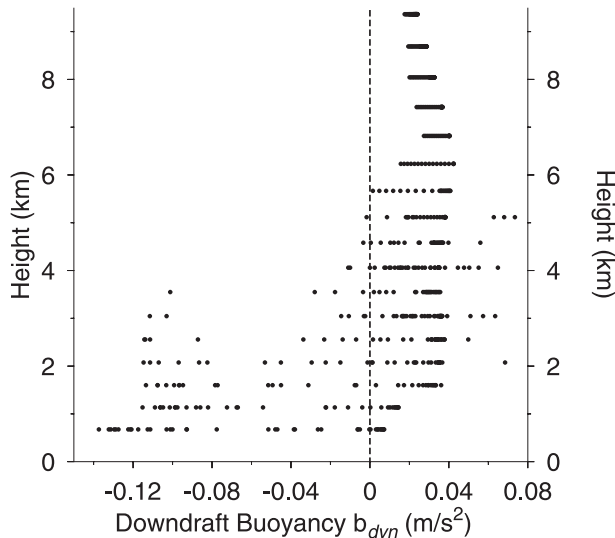
FIG. 5. The dynamical buoyancies b_{dyn} of downdraft parcels during one model time step.

FIG. 6. The diurnal average updraft (black solid), downdraft (black dashed), and radiative (gray solid) heating rates of the model.

cooling of rain shafts exiting clouds at these levels is focused into smaller fractional areas and, as shown in Fig. 5, generates downdraft parcel dynamical buoyancies that are negative. As a result, downdraft parcels move successively from one level to the next, advecting water vapor and other chemical tracers. This type of downdraft generates convective-scale downward motion and is referred to as "dynamic."

Figure 2 shows that, below 6 km, there is also a rapid increase in the rate of conversion of in-cloud rain to out-of-cloud rain. Changes in this conversion rate affect the magnitude of the downdraft evaporative cooling but have less effect on whether a downdraft is static or dynamic.

Static downdraft parcels do not themselves move between model levels but can have an indirect influence on the movement of updraft parcels. In radiative convective equilibrium, the temperatures tendencies at any model level must sum to zero. Increased evaporative cooling at any level must be balanced by some combination of decreased radiative cooling or increased updraft heating. Increased updraft heating is ordinarily associated with increased updraft mass flux.

b. Heating rates and diabatic mass fluxes

Figure 6 shows the heating rates associated with clear-sky radiation, updrafts, and downdrafts. In radiative convective equilibrium, $Q_r + Q_{up} + Q_{dn} = 0$. Updraft heating refers to the sum of temperature changes arising from induced subsidence, the evaporation of detrained updraft condensate, and the detrainment of updraft parcels whose temperature is different from the background temperature at that level. Similar considerations apply
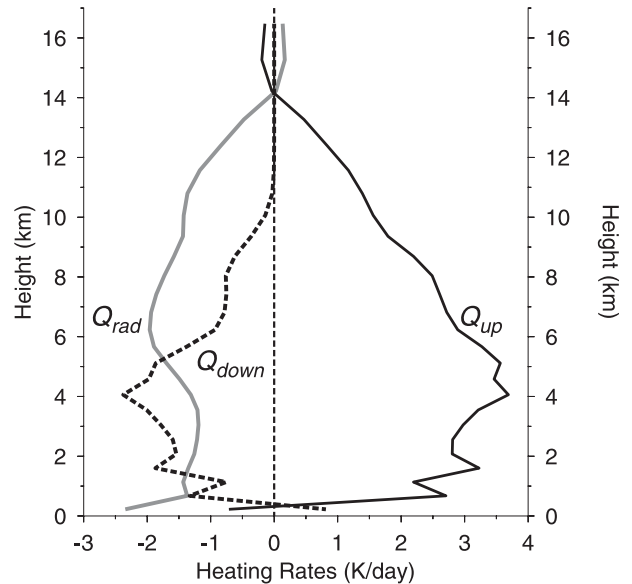
to the net temperature tendency from downdrafts. The downdraft cooling increases rapidly below 6 km. This is mainly a response to the prescribed increase in the in-cloud rain removal rate f_{rem}.

The diabatic, or cross-isentropic, mass flux of a heat source is equal to the heating rate divided by the local static stability σ. Figure 7 shows the updraft, downdraft, and radiative diabatic mass fluxes of the model.

Dynamic downdrafts cool the lower troposphere mainly by induced ascent. In this case, the convective downdraft mass flux ω_{dn} is approximately equal to the diabatic downdraft mass flux Q_{dn}/σ. Figures 4 and 7 indicate that these mass fluxes are, indeed, similar below the melting level.

The radiative mass flux divergence is given by

$$\delta_r = -\frac{\partial \omega_r}{\partial p}. \tag{38}$$

Figure 8 shows the diabatic mass flux divergence profiles associated with each of the three heat sources in the model. In the model, the mass flux divergence of the deep outflow mode between 10 and 15 km is balanced by the radiative mass flux convergence. The divergence of the congestus mode is balanced mainly by the melting-level downdraft convergence. The radiative mass flux divergence is weak between 2 and 8 km. In the model and observations (Folkins et al. 2008), the weakness of the vertical variation in the radiative mass flux in this interval is partly due to a covariation between the static stability and clear-sky radiative heating profiles.
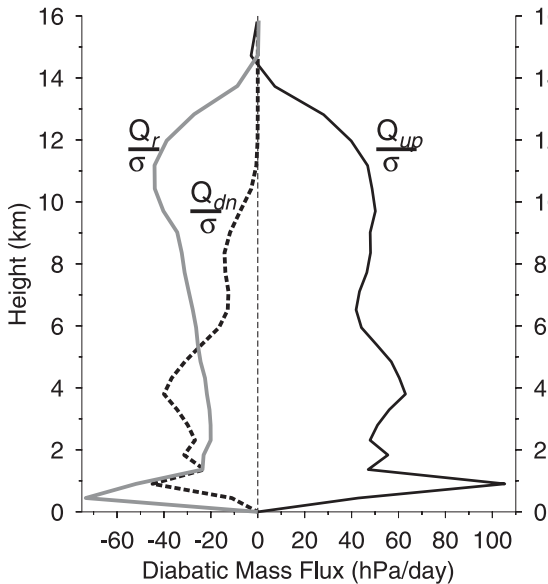
FIG. 7. The diabatic mass fluxes of the model due to updrafts Q_{up}/σ (solid black), downdrafts Q_{dn}/σ (dashed black), and radiation Q_r/σ (solid gray).

FIG. 8. The diabatic mass flux divergence due to updrafts δ_{up} (black solid), downdrafts δ_{dn} (black dashed), and radiation δ_r (gray solid).

c. Temperature profile

Figure 9 shows the deviation ΔT of the model temperature profile from a tropical climatology constructed from 14 SHADOZ radiosonde locations in the 20°S–20°N latitude band (Folkins and Martin 2005). The difference ΔT from the climatology is ~1 K below 13 km. The largest model errors occur near the tropopause. There is a ~6 K cold bias at 15 km. As discussed in a later section, this discrepancy is probably due to the convective heating profile of the model not extending to a sufficiently high altitude.

The left panel of Fig. 9 shows two lapse rate climatologies: one from SHADOZ and the other from Koror, an island within the west Pacific warm pool. It was obtained from the Stratospheric Processes and their Role in Climate (SPARC) radiosonde archive. The model is too unstable in the upper troposphere. Below 10 km, the lapse rate profile of the model is in good agreement with observations.

The gray curve in Fig. 9 is the lapse rate of a moist pseudoadiabat starting from the surface with $\theta_e = 352$ K. Both model and observations closely follow the pseudoadiabat from 6 to 10 km. The model also successfully reproduces the deviation of the observed lapse rate from the pseudoadiabat between 3 and 5 km (Mapes 2001; Folkins and Martin 2005). This deviation is referred to here as the melting-level stability anomaly (MLSA).

d. Relative humidity profile

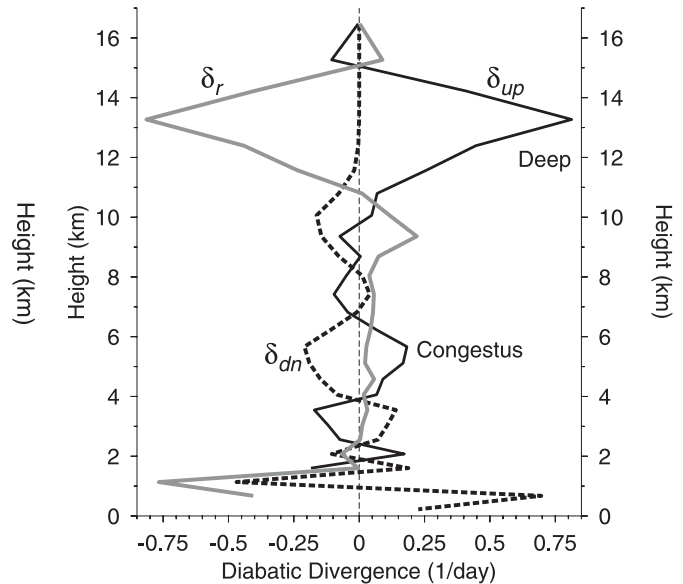Figure 10 is a comparison of the relative humidity profile generated by the model with several satellite and

radiosonde climatologies. The model successfully reproduces the overall C-shaped profile of tropical relative humidity. Some of this agreement arises from tuning. The model most accurately reproduces the slope and
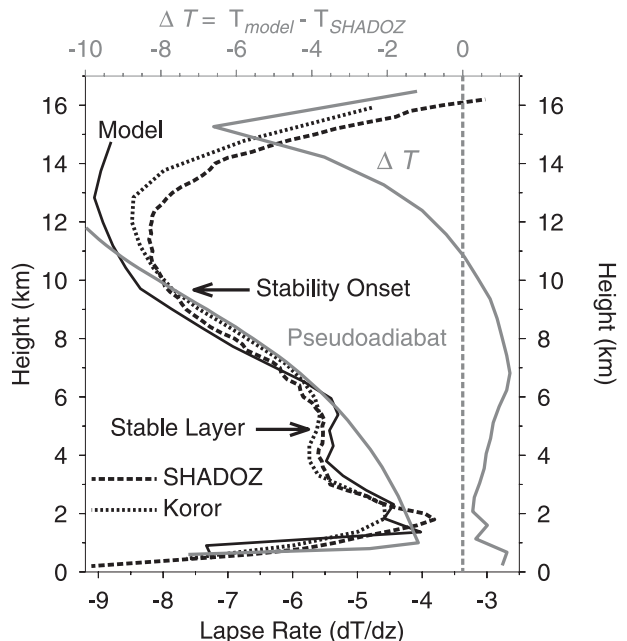

FIG. 9. The thick gray curve at right is the difference ΔT of the model temperature from the SHADOZ radiosonde climatology. The curves on the left show the lapse rate profiles (dT/dz) of the model (black solid), SHADOZ (black dashed), Koror (black dotted), and moist pseudoadiabat (gray solid).
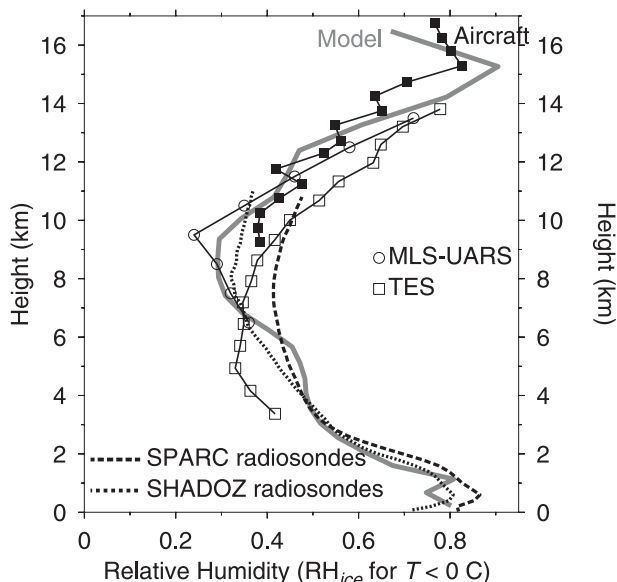
FIG. 10. The thick gray line is the relative humidity profile of the model. The other curves are relative humidity climatologies constructed from various measurements (Folkins et al. 2006): aircraft (solid squares), SPARC radiosonde (dashed), SHADOZ radiosonde (dotted), Microwave Limb Sounder (MLS) (Read et al. 2001) (open circles), and Tropospheric Emission Spectrometer (TES) (Beer 2006) (open squares). At temperatures below 0°C, the relative humidity is calculated with respect to the saturated vapor pressure of ice.

magnitude of observed relative humidities in the upper troposphere (10–15 km) when the maximum cloud condensate, as prescribed by Eq. (11), is set equal to a small fraction of the ambient saturated water vapor mixing ratio. In this region, the relative humidity profile of the model reflects a first-order balance between detrainment moistening and subsidence drying, as suggested by a previous diagnostic model (Folkins and Martin 2005).

Between 6 and 10 km, updraft detrainment is much weaker. In the absence of the larger values of updraft condensate, shown in Fig. 1, the relative humidity of the model in this height interval would be far too low. The retention of updraft condensate within tropical updrafts, to altitudes as high as 9 km ($\sim -20°C$), may reflect the inefficiency of rainfall production via collision and coalescence of water droplets below 9 km or the lack of ice condensation nuclei active at temperatures warmer than $-20°C$.

Below the melting level, the main source of moisture to the background atmosphere is updraft vapor detrainment. Downdrafts also increase the relative humidity of the lower troposphere through induced uplift and through the detrainment of parcels with higher relative humidity than the background value.

e. Comparison of cloud and rain properties with observations

Figure 1 shows that the updraft condensate in the model is roughly constant at 2.5 g kg^{-1} up to 8 km and then declines rapidly with height. This imposed variation is in rough agreement with observations. Liquid water content measurements within convective updrafts from aircraft suggest values of 0.5–1 g kg^{-1} up to 6 km followed by a rapid decrease with altitude (Jorgensen and LeMone 1989). Cloud water content measurements from *CloudSat* indicate larger values of 3–13 mg m^{-3} above the boundary layer, a peak in cloud water near 8 km, and a transition from liquid water to ice between 5 and 8 km (Su et al. 2008).

The out-of-cloud rain rate of the model is fixed at 100 mm day^{-1} below the melting level. It then decreases rapidly with height above the melting level. Measurements of the stratiform rain rate from the Tropical Rainfall Measuring Mission (TRMM) show a similar variation with height, except that the average stratiform rain rate below the melting level is $\sim$50 mm day^{-1} (Berg et al. 2002). Rain rates in the lower troposphere from convective precipitation are roughly 150 mm day^{-1}.

It is difficult to directly compare the imposed changes in rain shaft length with observations. However, this parameter has an effect on the amount of out-of-cloud rain. The evaporative moistening of longer rain shafts is focused over smaller areas, generates downdraft parcels of higher relative humidity, increases the likelihood of a rain shaft reaching the surface, and increases the out-of-cloud rain fraction. Figure 11 shows the vertical variation in the in-cloud and out-of-cloud rain. The ratio of out-of-cloud to in-cloud rain is roughly 1:3. Measurements from TRMM show that the proportion of stratiform to convective rain in the tropics between 2 and 4 km is roughly one to one (Takayabu 2002). This comparison suggests that the model underestimates out-of-cloud rain.

f. Diurnal cycle

The model simulations used a repetitive 24-h 1 June daily cycle at the equator. Due to solar heating during the day, atmospheric temperatures increase during the day and decrease at night. Figure 12 shows that the model has a $\sim$0.4 K diurnal variation in midtropospheric temperature, and a 1.6% variation in midtropospheric relative humidity (both averaged between 3 and 7 km). The diurnal variation in water vapor mixing ratio is small.

Over the oceans, tropical rainfall peaks at 0600 local time with an amplitude of 30% (Nesbitt and Zipser 2003). The black line in Fig. 12 shows the diurnal rainfall
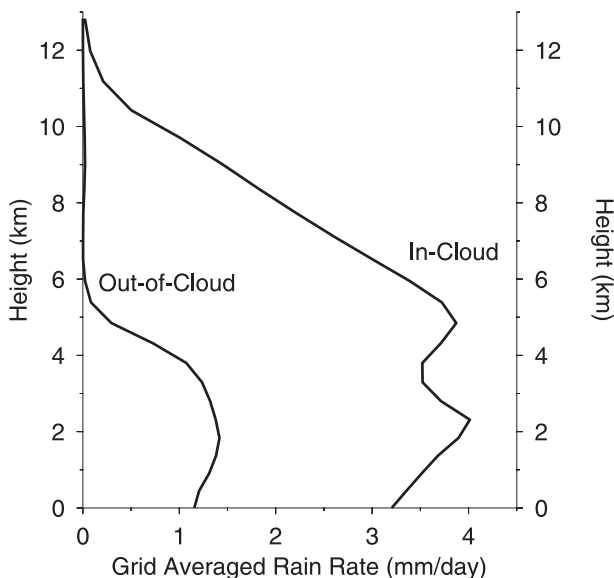
FIG. 11. The grid averaged in-cloud and out-of-cloud rain rates as a function of altitude.
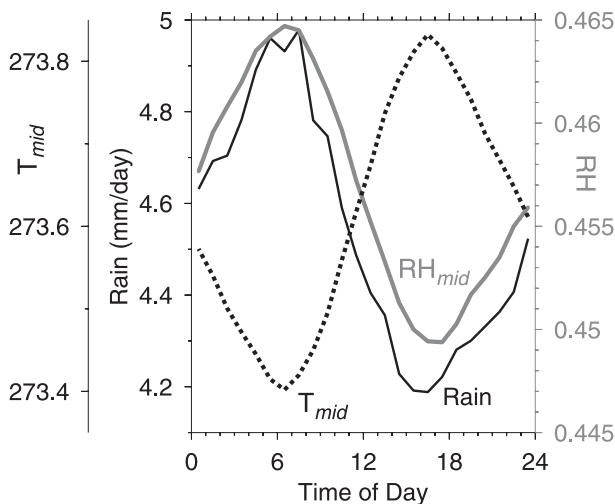

FIG. 12. The diurnal variation in surface rainfall (black solid), midtropospheric temperature T_{mid} (black dashed), and midtropospheric relative humidity RH_{mid} (gray solid): T_{mid} and RH_{mid} are averaged between 3 and 7 km.

variation in the model. The timing of the early morning rainfall peak in the model is consistent with observations. However, the modeled diurnal amplitude of 18% is smaller than the observed amplitude.

5. Discussion

a. Origin of the melting-level stability anomaly

Static downdrafts are those in which downdraft parcels are entrained from the background atmosphere, are moistened and evaporatively chilled by a rain shaft, and then detrain into the background atmosphere at the same level where they were entrained. For these types of downdrafts, it can be shown that the local cooling-to-moistening ratio of the background atmosphere associated with the downdraft is given by

$$\frac{dT}{dr_v} = \frac{-l_v(T)}{c_{pd} + r_v c_l}. \tag{39}$$

Figure 13 shows the vertical variation of the downdraft cooling-to-moistening ratio in the model. Above 6 km, where downdrafts are static, the vertical variation in this ratio is due to the temperature dependence of the latent heat of vaporization. Below 6 km, dynamic downdrafts introduce a low-level vertically overturning circulation in which the downdraft dT/dr_v ratio is no longer constrained by Eq. (39). The overall effect of downdrafts on the model becomes a nonlocal function of the downdraft parcel trajectories and the mean background r_v and h_m profiles of the model. For example, dynamic downdrafts

cool not only by the detrainment of evaporatively chilled air but also by induced ascent of the background atmosphere. Comparison of Figs. 4 and 13 indicates that the downdraft dT/dr_v ratio tends to be reduced just below the melting level where downdrafts are convergent and increased below 4 km where downdrafts are divergent. The enhanced cooling just below the melting level destabilizes the tropical lower troposphere and brings the lapse rate profile of the model into better agreement with observations.
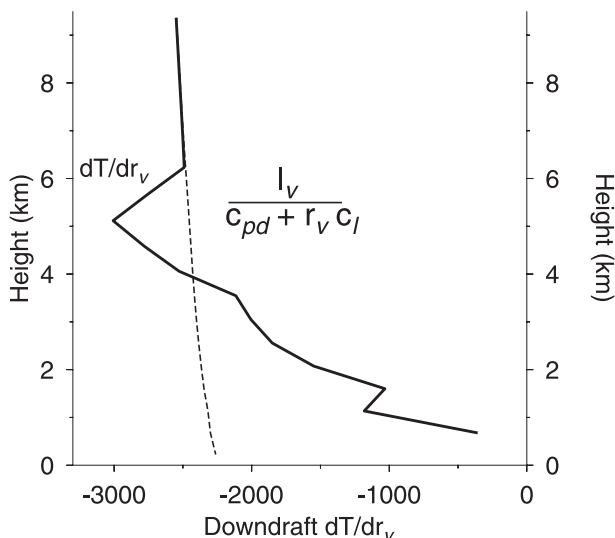

FIG. 13. The solid curve shows the downdraft cooling-to-moistening ratio of the model. The dashed line denotes $l_v/(c_{pd} + r_v c_l)$, the cooling-to-moistening ratio expected for static downdrafts.

The melting level stability anomaly (MLSA) shown in Fig. 9 could also be reproduced using static downdrafts simply by tuning the vertical variation of the in-cloud rain removal rate f_{rem} to the observed stability profile. In this case, however, the relative humidity of the model near the melting level would be significantly larger than the observed climatology. In the model, simultaneous agreement with both observed relative humidity and stability profiles can only be obtained by a transition from static to dynamic downdrafts at the melting level in which there is a change in the downdraft dT/dr_v ratio.

The amount of evaporation in the model is mainly controlled by the in-cloud rain shaft removal rate f_{rem}. The buoyancy of downdraft parcels, and in particular whether they are static or dynamic, is mainly determined by the out-of-cloud rain rate rn_{rate} and rain shaft length dz_{rain}. Above the melting level, changes in the vertical variation of rn_{rate} and dz_{rain} that do not generate dynamic downdrafts have no effect on the downdraft dT/dr_v ratio. Such changes therefore also have no effect on the mean temperature or relative humidity profiles of the model. Similarly, below the melting level, where all downdrafts are to some degree dynamic, the effects of modest changes in rn_{rate} and dz_{rain} on the background temperature and relative humidity are small. The strategy adopted here was to impose a vertical variation in rn_{rate} that represented a rough compromise between observed stratiform and convective rain rates. The imposed vertical variation in dz_{rain} should be viewed as a particular mechanism in the model to force a static to dynamic downdraft transition at the melting level, rather than as an attempt to realistically represent an actual vertical variation in rain shaft geometry.

b. Origin of the congestus and deep outflow modes

Figure 14 shows a vertical profile of the updraft mixing coefficients σ_{back} and σ_{for} from one time step of a model run. At any given level, the signs of σ_{for} and σ_{back} may be opposite, so an updraft parcel may both entrain and detrain at the same altitude.

At the starting level, updraft parcels are initialized with an h_{mp} spectrum given by Eq. (10). As they rise in the atmosphere, the most energetic updraft parcels have the largest positive buoyancies, the largest buoyancy gradients, and therefore would tend to have the largest mixing coefficients. However, the updraft mixing coefficients given in Eq. (13) are also inversely proportional to the updraft index n_l so that, in practice, the most energetic updrafts have the smallest mixing coefficients.

The entrainment and detrainment of updraft parcels is governed by the local buoyancy gradient. Figure 9 shows that, between 2 and 4 km, the lapse rate of the model becomes progressively unstable with respect to
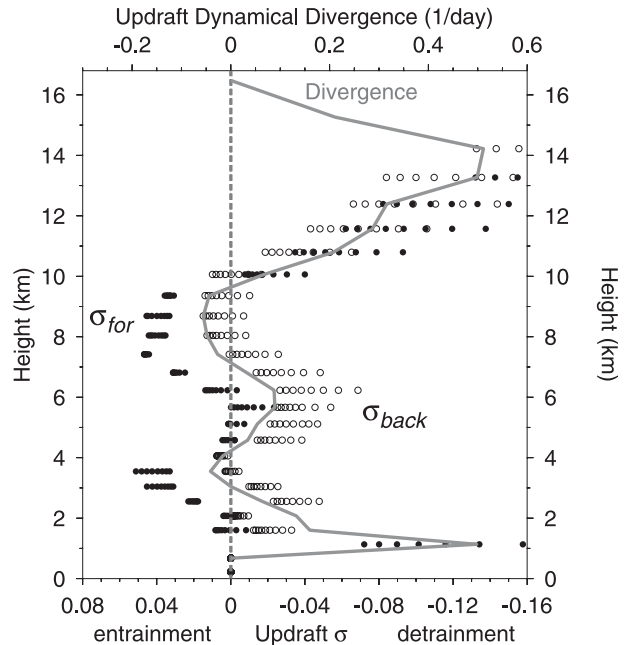

FIG. 14. The thick gray curve shows the trimodal updraft divergence (detrainment–entrainment) of the model. Peaks in convective outflow occur at 2 km, 6 km, and 13 km. Filled black circles represent the forward mixing fractions σ_{for} of various updraft parcels. The open circles represent the backward mixing fraction σ_{back}. The mixing fractions are per model interval (approximately 0.5 km near the surface, 1.0 km near 15 km). The x axis goes from positive to negative σ.

the pseudoadiabat, which approximates the undilute density profile of the updrafts. In this height interval, the buoyancy of rising updraft parcels increases, so, as shown in Fig. 14, their mixing coefficients progressively favor entrainment. This tendency is reversed at 4 km where the modeled lapse rate profile starts to again approach the pseudoadiabat. As a result, the buoyancy of updraft parcels is reduced, their mixing coefficients become progressively more negative, and they preferentially detrain. The gray curve in Fig. 14 shows the updraft mass flux divergence $-\partial\omega_{up}/\partial p$ of the model. The congestus peak occurs at 6 km, near the top of the MLSA where the lapse rate of the model has rejoined the pseudoadiabat and detrainment is strongest.

Similar considerations apply to the deep outflow mode. The lapse rate of the model becomes increasingly stable with respect to the pseudoadiabat above 10 km. Updraft parcels detrain as they encounter this stability layer. This detrainment contributes to the large values of updraft divergence between 10 and 16 km.

Figure 15 shows the trajectories of updraft parcels in the moist static energy–mass $(h_m - m_{d,up})$ plane. The maximum number of parcels launched from the boundary layer during one time step (n_{launch}) is equal to 16.
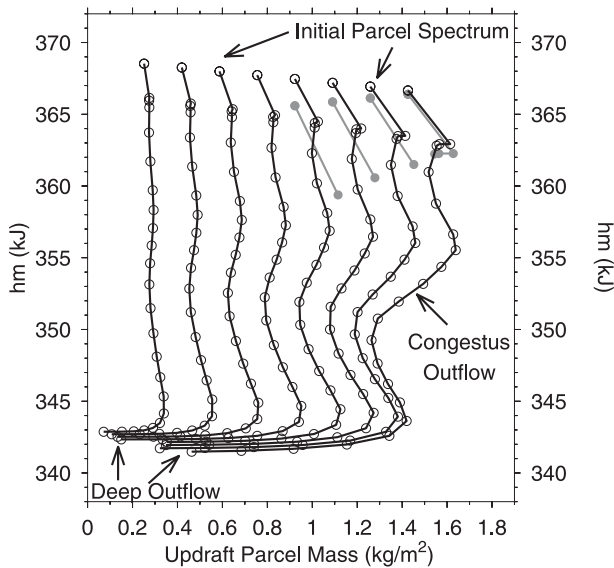
FIG. 15. A projection of 12 updraft parcel trajectories during one model time step on to the moist static energy and dry mass ($h_m - m_{dp}$) plane.

However, the four parcels with the smallest h_m do not have positive $cape_d$ and are not subjected to an initial ascent. The eight parcel trajectories shown in black have larger initial h_m than the four trajectories shown in gray. All trajectories start at the lowest model level. Parcel h_m decreases in response to entrainment and loss of condensate (formation of precipitation). Parcel mass increases (decreases) in response to entrainment (detrainment). The mass of the most energetic parcels is virtually constant until several kilometers below their final detrainment height, indicating that their loss of moist static energy with altitude is almost entirely due to loss of condensate rather than mixing. The most energetic, but least massive, parcels detrain at highest final h_m and highest altitude. Reductions in parcel mass for $h_m <$ 345 kJ are associated with the deep outflow mode. Reductions in parcel mass for $h_m < 355$ kJ are associated with the congestus mode.

Figure 14 shows that the congestus mode has a maximum divergence of ~0.2 day^{-1} and extends from 4 to 6.5 km. It is difficult to diagnostically infer the strength of the congestus mode from sounding observations. This is partly because, within a sounding array consisting of a mixture of cloud types, the divergence of the congestus mode can be offset by the melting-level convergence of rainy stratiform anvils. However, a sounding budget analysis near the Marshall Islands suggests an average peak divergence of 2×10^{-6} s^{-1} (0.17 day^{-1}) near 500 hPa, with net divergence between 650 (3.5 km) and 400 hPa (7.5 km) (Schumacher et al. 2008).

c. Updraft mixing and the upper-tropospheric cold bias

In the tropics, convection is enhanced over areas of the ocean with high sea surface temperatures and over land. The spatial separation between areas of preferred convection and areas of preferred subsidence is associated with the Hadley–Walker circulation in which convection tends to occur under conditions of large-scale low-level convergence and upper-level divergence. On smaller spatial scales, within actively convecting regions, deep convection preferentially develops under conditions of enhanced low-level humidity (Sherwood 1999). The spatial and temporal variability of tropical convection can be expected to be associated with nonlinearities, which make it difficult to reproduce some aspects of the tropical mean state within the context of a one-dimensional steady-state model with no external forcing.

The model has little rainfall variance other than associated with the diurnal cycle. Deep convection therefore occurs in a background atmosphere that approximates the tropical mean. As a result, the entrainment of background air by updraft parcels reduces updraft moist static energy more rapidly than would occur within real deep-convective updrafts. The model attempts to compensate for the lack of lower-tropospheric moisture variance by reducing the mixing of the updraft parcels with the highest energy. If this were not done, deep convective outflow would still occur, but the variance in the updraft moist static energy and buoyancy spectrum would be much smaller, and the vertical width of the deep outflow profile shown in Fig. 8 would be reduced. It is likely, however, that despite the reduction in the mixing of the highest energy updraft parcels, the amount of very high convective outflow in the model is too weak. Diagnostic studies suggest that the updraft diabatic divergence profile extends to 17 km (Folkins and Martin 2005). However, Fig. 8 shows that the updraft diabatic divergence profile of the model is negative above 15 km. The lack of very high altitude convective outflow in the model contributes to the upper-tropospheric cold bias shown in Fig. 9.

d. Updraft buoyancies and the origin of the diurnal cycle

Figure 16 shows a mass-weighted probability distribution of the difference between the density temperature of the updraft parcels and the background atmosphere between 3 and 7 km. The density temperature incorporates the effects of changes in temperature, water vapor mixing ratio, and condensate loading on updraft buoyancy. In the model, the temperature excess ranges from −0.3 to 1.5 K. Observed values of virtual
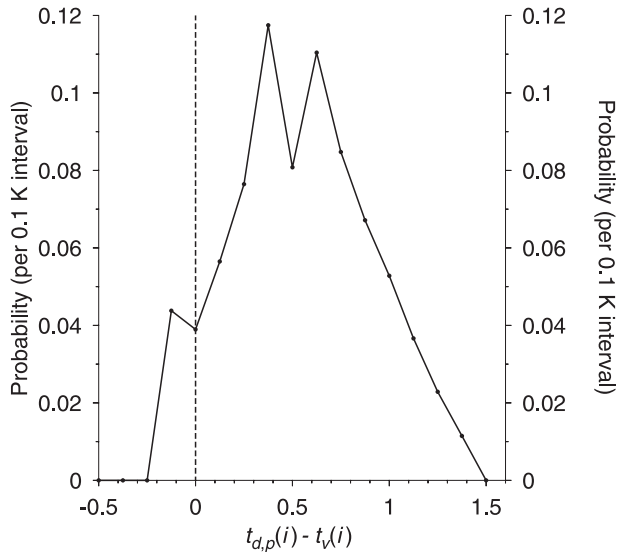
FIG. 16. The mass-weighted probability distribution of the updraft density temperature excess between 3 and 7 km in the model. The temperature excess is defined as $T_{d,p}(i) - T_v(i)$, where $T_{d,p}(i)$ is the parcel density temperature at level i, and $T_v(i)$ is the virtual temperature of the background atmosphere at level i.

temperature excess within tropical updrafts range from -1.5 to 3.0 K (Jorgensen and LeMone 1989).

Figure 12 shows that the diurnal variation in midtropospheric temperatures of the model is roughly 0.4 K. As shown in Fig. 16, the temperature excess probability near zero buoyancy is roughly 6.0% per 0.1 K interval. An increase in midtropospheric temperatures of 0.4 K would therefore be expected to give rise to an approximately 24% reduction in midtropospheric mass flux in the absence of any other changes in updraft properties. This is similar to the modeled diurnal rainfall variation in the model of 18%. This comparison suggests that the ability of a model to replicate the diurnal rainfall cycle over the ocean may also be a test of its ability to replicate the observed updraft buoyancy distribution. Rainfall generated by weakly buoyant updrafts should be more sensitive to perturbations in background atmospheric temperatures associated with the diurnal cycle.

6. Summary

We have described a buoyancy-based parcel model that is able to generate realistic profiles of relative humidity, lapse rate, and congestus outflow in the tropical lower troposphere. The melting-level stability anomaly (MLSA) had been previously reproduced using a one-dimensional model subjected to a large-scale forcing (Bony and Emanuel 2001). In this model, it is reproduced without an external forcing. The lapse rate anomaly is due to the existence of a stratiform downdraft

circulation below the melting level. This circulation modifies the cooling-to-moistening ratio associated with evaporative downdrafts and destabilizes the tropical lower troposphere.

In the model, the transition from static to dynamic downdrafts at the melting level is driven by prescribed changes in the out-of-cloud rain rate and rain shaft length. The imposed change in rain rate is based on observations. The imposed change in rain shaft length is not directly comparable with observations. This change is needed to increase the time over which downdraft parcels are exposed to evaporation from falling rain. The imposed increase in rain rate at the melting level would not, by itself, be sufficient to generate dynamic downdrafts. It is possible that, in reality, there is indeed some increase in the vertical coherence of out-of-cloud rain shafts at the melting level that increases the negative buoyancy of stratiform downdrafts. The model simulations strongly suggest that some change in the cooling-to-moistening ratio of downdrafts is required at the melting level to explain the observed mean temperature and relative humidity profiles. However, the particular mechanism adopted by the model to trigger this change is to some degree incidental. It is perhaps more likely that, owing to the large horizontal area of rainy stratiform clouds, the production of dynamic downdrafts below the melting level is due to the repetitive exposure of downdraft parcels to multiple rain shafts as they are advected under stratiform anvils.

Although there are other explanations (Posselt et al. 2008), congestus outflow has most often been attributed to the existence of stable layers near the melting level (Johnson et al. 1999; Redelsperger et al. 2002). When updraft parcels encounter these levels, they lose buoyancy and (sometimes) detrain. The buoyancy-based updraft detrainment parameterization adopted in this paper produces congestus outflow in a manner consistent with this explanation. The efficacy of this mechanism does not require that the stability of the atmosphere increase with height (though it may), only that the density of the background atmosphere decrease with height less rapidly than that of the updraft parcels themselves. These conditions are favored by the presence of the MLSA.

The explanation given above for the existence of the congestus mode is the explanation most relevant to the dynamical evolution and mixing of an individual convective cloud. However, the stability anomaly is generated by stratiform downdrafts. This introduces a coupling between the melting-level stratiform downdraft convergence and the congestus divergence. Just as one can think of the divergence of the deep outflow mode as being balanced, on large scales, by the radiative mass flux convergence of the background atmosphere, it may

be appropriate to think of the congestus divergence as being mainly balanced, and to some extent perhaps controlled, by the stratiform downdraft melting-level convergence. It is difficult to address this question without some knowledge of the spatial and/or temporal scale over which heat sources give rise to circulations in the tropical atmosphere. This issue is beyond the scope of a one-dimensional model. However, radiosonde winds have been used to show that the dynamical divergence (i.e., the divergence computed directly from the wind field) is near zero in actively convecting regions of the tropics between roughly 2 and 7 km on spatial scales >1000 km (Folkins et al. 2008). This suggests that the melting-level convergent inflow into deep convective systems is progressively screened at larger spatial scales by the divergent outflow from a surrounding population of cumulus congestus. This gives rise to a closed regional-scale lower-tropospheric circulation that is roughly four times smaller than the deep Hadley circulation (Folkins et al. 2008; Posselt et al. 2008). The existence of a coupling between the melting-level downdraft convergence and the congestus divergence may be an important aspect of tropical predictability. The induced environmental uplift associated with stratiform downdrafts destabilizes the atmosphere, creating conditions favorable for the subsequent growth of nearby congestus clouds (Mapes 1993). In turn, these congestus clouds provide the premoistening that typically precedes the development of deep convection (Sherwood 1999).

REFERENCES

Beer, R., 2006: TES on the Aura mission: Scientific objectives, measurements and analysis overview. *IEEE Trans. Geosci. Remote Sens.,* **44,** 1102–1105.

Berg, W., C. Kummerow, and C. A. Morales, 2002: Differences between east and west Pacific rainfall systems. *J. Climate,* **15,** 3659–3672.

Bony, S., and K. A. Emanuel, 2001: A parameterization of the cloudiness associated with cumulus convection: Evaluation using TOGA COARE data. *J. Atmos. Sci.,* **58,** 3158–3183.

Bretherton, C. S., and P. K. Smolarkiewicz, 1989: Gravity waves, compensating subsidence and detrainment around cumulus clouds. *J. Atmos. Sci.,* **46,** 740–759.

Emanuel, K. A., 1991: A scheme for representing cumulus convection in large-scale models. *J. Atmos. Sci.,* **48,** 2313–2335.

——, 1994: *Atmospheric Convection.* Oxford University Press, 580 pp.

——, and M. Zivkovic-Rothman, 1999: Development and evaluation of a convection scheme for use in climate models. *J. Atmos. Sci.,* **56,** 1766–1782.

Folkins, I., and C. Braun, 2003: Tropical rainfall and boundary layer entropy. *J. Climate,* **16,** 1807–1820.

——, and R. V. Martin, 2005: The vertical structure of tropical convection, and its impact on the budgets of water vapor and ozone. *J. Atmos. Sci.,* **62,** 1560–1573.

——, and Coauthors, 2006: Testing convective parameterizations with tropical measurements of HNO_3, CO, H_2O, and O_3: Implications for the water vapor budget. *J. Geophys. Res.,* **111,** D23304, doi:10.1029/2006JD007325.

——, S. Fueglistaler, G. Lesins, and T. Mitovski, 2008: A low-level circulation in the tropics. *J. Atmos. Sci.,* **65,** 1019–1034.

Fowler, L. D., D. A. Randall, and S. A. Rutledge, 1996: Liquid and ice cloud microphysics in the CSU general circulation model. Part I: Model description and simulated microphysical processes. *J. Climate,* **9,** 489–529.

Fu, Q., and K. N. Liou, 1992: On the correlated k-distribution method for radiative transfer in nonhomogeneous atmospheres. *J. Atmos. Sci.,* **49,** 2139–2156.

Fueglistaler, S., A. E. Dessler, T. J. Dunkerton, I. Folkins, Q. Fu, and P. W. Mote, 2009: Tropical tropopause layer. *Rev. Geophys.,* **47,** RG1004, doi:10.1029/2008RG000267.

Gregory, D., and P. R. Rowntree, 1990: A mass flux scheme with representation of cloud ensemble characteristics and stability-dependent closure. *Mon. Wea. Rev.,* **118,** 1483–1506.

Inness, P. M., J. M. Slingo, S. J. Woolnough, R. B. Neale, and V. D. Pope, 2001: Organization of tropical convection in a GCM with varying vertical resolution: Implications for the simulation of the Madden-Julian Oscillation. *Climate Dyn.,* **17,** 777–793.

Johnson, R. H., T. M. Rickenbach, S. A. Rutledge, P. E. Ciesielski, and W. H. Schubert, 1999: Trimodal characteristics of tropical convection. *J. Climate,* **12,** 2397–2418.

Jorgensen, D. P., and M. A. LeMone, 1989: Vertical velocity characteristics of oceanic convection. *J. Atmos. Sci.,* **46,** 621–640.

Kuang, Z., and C. S. Bretherton, 2006: A mass-flux scheme view of a high-resolution simulation of a transition from shallow to deep cumulus convection. *J. Atmos. Sci.,* **63,** 1895–1909.

Liu, C., and M. W. Moncrieff, 1998: A numerical study of the diurnal cycle of tropical oceanic convection. *J. Atmos. Sci.,* **55,** 2329–2344.

Mapes, B. E., 1993: Gregarious tropical convection. *J. Atmos. Sci.,* **50,** 2026–2037.

——, 2001: Water's two scale heights: The moist adiabat and the radiative troposphere. *Quart. J. Roy. Meteor. Soc.,* **127,** 2353–2366.

——, and R. A. Houze, 1995: Diabatic divergence profiles in western Pacific mesoscale convective systems. *J. Atmos. Sci.,* **52,** 1807–1828.

Nesbitt, S. W., and E. J. Zipser, 2003: The diurnal cycle of rainfall and convective intensity according to three years of TRMM measurements. *J. Climate,* **16,** 1456–1475.

Posselt, D. J., S. C. van den Heever, and G. L. Stephens, 2008: Trimodal cloudiness and tropical stable layers in simulations of radiative convective equilibrium. *Geophys. Res. Lett.,* **35,** L08802, doi:10.1029/2007GL033029.

Read, W. G., and Coauthors, 2001: UARS Microwave Limb Sounder upper tropospheric humidity measurement: Method and validation. *J. Geophys. Res.,* **106,** 32 207–32 258.

Redelsperger, J.-L., D. B. Parsons, and F. Guichard, 2002: Recovery processes and factors limiting cloud-top height following the arrival of a dry intrusion observed during TOGA COARE. *J. Atmos. Sci.,* **59,** 2438–2457.

Rosenlof, K. H., and J. R. Holton, 1993: Estimates of the stratospheric residual circulation using the downward control principle. *J. Geophys. Res.,* **98,** 10 465–10 479.

Schumacher, C., P. E. Ciesielski, and M. H. Zhang, 2008: Tropical cloud heating profiles: Analysis from KWAJEX. *Mon. Wea. Rev.,* **136,** 4289–4300.

Sherwood, S. C., 1999: Convective precursors and predictability in the tropical western Pacific. *Mon. Wea. Rev.,* **127,** 2977–2991.

Su, H., J. H. Jiang, D. G. Vane, and G. L. Stephens, 2008: Observed vertical structure of tropical oceanic clouds sorted in large-scale regimes. *Geophys. Res. Lett.,* **35,** L24704, doi:10.1029/2008GL035888.

Takayabu, Y. N., 2002: Spectral representation of rain profiles and diurnal variations observed with TRMM PR over the equatorial area. *Geophys. Res. Lett.,* **29,** 1584, doi:10.1029/2001GL014113.

Thompson, A. M., and Coauthors, 2003: Southern Hemisphere Additional Ozonesondes (SHADOZ) 1998–2000 tropical ozone climatology 1. Comparison with Total Ozone Mapping Spectrometer (TOMS) and ground-based measurements. *J. Geophys. Res.,* **108,** 8238, doi:10.1029/2001JD000967.